Research Square

Preprints are preliminary reports that have not undergone peer review.
They should not be considered conclusive, used to inform clinical practice,
or referenced by the media as validated information.

Metallic Transport in a Polymer-Based Negative Bipolaron Network

Reverant Crispin

reverant.crispin@liu.se

Linköping University

Shaohua Tong

South China University of Technology https://orcid.org/0009-0000-5668-8041

Hanlin Gan

South China University of Technology

Mengming Sun

South China University of Technology

Hongchao Peng

South China University of Technology

Zhenghua Qu

South China University of Technology

Wei Cui

South China University of Technology

Yanuo Zhu

South China University of Technology

Jiaji Yang

South China University of Technology

Hio-Ieng Un

South China University of Technology https://orcid.org/0000-0003-4242-3573

Liang Yao

South China University of Technology

Nan Zheng

South China University of Technology

Haoran Tang

South China University of Technology https://orcid.org/0000-0002-0963-7230

Jiang Zhang

South China University of Technology https://orcid.org/0000-0002-1574-5406

Fei Huang

South China University of Technology https://orcid.org/0000-0001-9665-6642

Qinglin Jiang

South China University of Technology

Yuguang Ma

South China University of Technology https://orcid.org/0000-0003-0373-5873

Article

Keywords:

Posted Date: June 29th, 2026

DOI: https://doi.org/10.21203/rs.3.rs-9934094/v1

License: This work is licensed under a Creative Commons Attribution 4.0 International License.
Read Full License

Additional Declarations: There is **NO** Competing Interest.

Abstract

Metallic conductivity in conducting polymers is exceptional[1] and was found under p-doped systems[2–5], enabled by interchain percolation pathways[6] that support extended charge-carrier delocalization. Achieving analogous metallic transport in n-doped conjugated polymers remains a major challenge. In poly(benzodifurandione) (PBFDO), high conductivity has been reported, yet definitive evidence of a genuine metallic state and the nature of the doping charges remain unresolved[7–10]. Prevailing models associate metallic transport with delocalized negative polaron networks, while negative bipolaron lattices are expected to yield semiconducting or at most semimetallic behaviour. Here we demonstrate that PBFDO exhibits genuine metallic conductivity over a broad temperature range from 300 K down to 20 K, as evidenced by a positive temperature coefficient of resistance throughout. Ionic-liquid treatment further strengthens this metallic response, with conductivity exceeding 20,000 S cm^{-1} at 10 K. This metallic state originates from a negative bipolaron network stabilized by proton reorganization, supported by suppressed electron paramagnetic resonance signals and a pronounced Drude-like infrared response. Electronic structure calculations of the bipolaron network reveal partially filled dispersive bands crossing the Fermi level, consistent with a true metallic state.

Introduction

Semiconducting polymers exhibit broad intrachain bands (>1 eV) and much narrower interchain bands (<0.3 eV), and their strong electron–phonon coupling can localize charge carriers into polarons despite their intrinsically delocalized electronic structure[11]. A polaron is a charged lattice distortion, whose sign depends on whether an electron is removed from the valence band (VB, positive polaron) or added to the conduction band (CB, negative polaron)[12]. The spatial extent of charge localization over a few monomer units depends on both the number of excess charges associated with the defect—one for a polaron and two for a bipolaron—and the presence of nearby counterions that stabilize the charged state[13].

Fig. 1| Electronic structure of n- and p-doped charge species and the resulting delocalized bands at high doping levels in the presence of significant interchain coupling. a, Positive polaron (radical cation). **b**, Positive polaron network is a metal with a half-filled, delocalized positive polaron band. **c**, Negative polaron (radical anion). **d**, Negative polaron network is a metal with a half-filled, delocalized negative polaron band at high energy. **e**, Positive bipolaron (dication). **f**, Positive bipolaron network is a semimetal with the empty low-energy bipolaron band overlapping with the top of a modified valence band (modified means it is not the VB of the undoped system). **g**, Negative bipolaron (dianion). **h**, Negative bipolaron network is a semimetal with the formation of a delocalized negative bipolaron band overlapping with a modified empty conduction band.

The charged lattice distortion is typically identified by the emergence of two new electronic states within the band gap. The low-energy (bi)polaronic level (LEP or LEBP) originates from the destabilization of the top of the valence band of the neutral polymer (highest occupied molecular orbital, HOMO), whereas the high-energy (bi)polaronic level (HEP or HEBP) arises from the stabilization of the bottom of the

conduction band (lowest unoccupied molecular orbital, LUMO). The presence of these intragap (bi)polaronic levels gives rise to additional optical transitions[14]. In general, doubling the charge within a single geometric defect induces a larger structural distortion, resulting in a more pronounced modification of the bond-length alternation around the excess charge. Consequently, LEBP is often higher in energy than LEP, and HEBP is often lower in energy than HEP[15]. These intragap electronic levels occur for both positive and negative (bi)polarons, and their energies depend on their electronic occupation as well as other energetic contributions. A positive polaron (radical cation) carries a spin of 1/2, with LEP singly occupied and HEP empty (Fig. 1a). A positive bipolaron (dication) is spinless, with both LEBP and HEBP remaining empty (Fig. 1e). A negative polaron (radical anion) also carries a spin of 1/2, with LEP doubly occupied and HEP singly occupied (Fig. 1c), whereas a negative bipolaron (dianion) is spinless, with both LEBP and HEBP fully occupied (Fig. 1g).

Increasing the doping level up to approximately one excess charge every two to five monomer units enhances the electrical conductivity by many orders of magnitude, reaching values from hundreds to thousands of S cm^{-1} for both p-doped[16] and n-doped polymers[8,17]. This dramatic increase arises not only from the higher charge-carrier density but, more importantly, from the overlap and flattening of the electrostatic potentials associated with the counterions, which leads to a substantial increase in charge-carrier mobility[18]. At such high doping levels, the electronic structure is profoundly transformed: the (bi)polaronic states become sufficiently dense to merge into a band, while the original conduction and valence bands are strongly perturbed. As a consequence, the electronic structure of the highly doped polymer bears little resemblance to that of the undoped system.

When the local structural order increases, however, interchain electronic coupling can delocalize the polaron wavefunction within percolated crystalline nanodomains, thereby generating an energy dispersion in a half-filled band and enabling metallic transport. The metallic conductivity observed in highly ordered, p-doped polyaniline films was rationalized by the formation of a half-filled, delocalized positive polaron band at low energy (Fig. 1b)[2,4,5]. Metallic transport is macroscopically characterized by a decrease in conductivity upon heating, indicating dominant charge-carrier scattering by phonons. In highly ordered, p-doped poly(3,4-ethylenedioxythiophene) (PEDOT), the empty low-energy bipolaron band overlaps with the top of the modified valence band, giving rise to a p-doped polymer semimetal that also exhibits metallic conductivity and enhanced Seebeck coefficient (Fig. 1f)[3].

To date, no experimental evidence has been reported for the n-doped analogue, namely a half-filled, delocalized negative polaron band at high energy (Fig. 1d). Likewise, the potential existence of an n-doped polymer semimetal—implying the formation of a delocalized negative bipolaron band overlapping with an empty conduction band (Fig. 1h)—remains an open question. Early theoretical work proposed the possibility of forming negative bipolaron bands in n-doped polymers through the filling of HEBP or HEP levels upon electron doping[19]. These occupied HEBP and HEP states were later directly probed by ultraviolet photoelectron spectroscopy in poly(para-phenylenevinylene) doped in vacuum with sodium atoms as a reducing agent[20]. Recent advances in the high-conductivity n-type polymer

poly(benzodifurandione) (PBFDO) have significantly narrowed this gap, yet the nature of the doping species leading to metallic conduction has remained elusive[7].

Here, we report unequivocal evidence of metallic conductivity in n-type PBFDO films, demonstrated by a positive temperature coefficient of resistance and ultrahigh electrical conductivity of > 20,000 S cm^{-1} at 10 K. The films were investigated using a comprehensive suite of experimental techniques, revealing the interplay among spin, crystallographic order, and optical, thermoelectric, and magnetoelectronic properties. We show that ionic liquid post-treatment promotes reorganization of protonation sites along the PBFDO chains, thereby driving bipolaron formation over polaronic species. In its most energetically favorable protonation state, PBFDO exhibits a nearly undetectable EPR signal, consistent with the emergence of a negative bipolaron network. Three-dimensional band-structure calculations on this bipolaron network reveal the formation of a partially filled band that indicates a true metallic state rather than the semimetallic behaviour suggested by the simplified model in Fig. 1h.

Results

Because proton involvement is central to this work, we briefly recall the chemical steps underlying the n-doping mechanism as described in the literature[7]. Oxidative polymerization is initiated when duroquinone (TMQ) accepts two electrons and two protons from the H-BFDO monomer, yielding the polymer PBFDO while TMQ is reduced to its diol form, H-TMQ. The redox potential of the TMQ/H-TMQ couple ($TMQ + 2e^- + 2H^+ \rightarrow$ H-TMQ) is such that, once the low-bandgap polymer PBFDO is formed, H-TMQ spontaneously reduces it to the n-doped polymer H-PBFDO, which is soluble in DMSO. In this process, protons (H^+) act as counterions to the negative charges delocalized along the π-conjugated $PBFDO^-$ backbone. For the sake of simplicity, we use the notation PBFDO for the proton-compensated n-doped polymer. While the overall polymerization mechanism is established, the doping mechanism has remained insufficiently explored and exploited. The PBFDO solution (10 mg mL^{-1} in DMSO) was synthesized as previously reported[7]. After spin-coating the solution on a prepatterned quartz substrate with gold electrodes separated by a 2-μm channel, the films were dried in an inert atmosphere and vacuum annealed to remove the solvent.

The normalized resistance, measured with a four-electrode setup (relative to 300 K) exhibits a clear positive temperature coefficient ($dR/dT > 0$) over the entire measured range from 300 K down to 20 K (Fig. 2a). This behaviour constitutes an unambiguous hallmark of metallic transport and clearly differentiates PBFDO from previously reported systems. In earlier studies, transport was predominantly thermally activated, characteristic of semiconducting behaviour[21], or located within the critical regime of the insulator–metal transition, where metallic conduction emerged only above ~ 270 K, while semiconducting behaviour remained dominant at lower temperatures[7,8]. Notably, the films exhibit an exceptionally low residual-resistance ratio (RRR, $R(20\ K)/R(300\ K) \approx 0.44$), which highlights the preservation of high charge-transport efficiency at cryogenic temperatures, approaching the metallic behaviour reported for p-doped polyaniline (RRR ≈ 0.40)[2]. Among the catalysts investigated, films

prepared with TMQ yielded the most pronounced metallic response, although other catalysts also exhibited clear metallic character (Fig. S1)[8,9].

The metallic character of spin-coated PBFDO films is further corroborated by the strictly linear temperature dependence of the Seebeck coefficient (Fig. 2b), consistent with metallic charge transport described by the extended Drude model in conjunction with the Mott formula[22,23]. The Mott formalism accounts for broken electron-hole symmetry around the Fermi level and for the energy dependence of charge-carrier mobility, yielding a small but finite thermopower in metals (typically 1–10 $\mu V K^{-1}$) and larger values in semimetals (≈ 10–200 $\mu V K^{-1}$)[24,25]. In conducting polymers, however, macroscopic charge transport is fundamentally constrained by the narrow interchain electronic bandwidth (typically < 0.3 eV), governed by weak π-π coupling rather than the strong atomic orbital overlap characteristic of inorganic (semi)metals. As a result, the energy dependence of the density of states near the Fermi level is comparatively smooth, which intrinsically limits the magnitude of the Seebeck coefficient. This explains why the semimetal PEDOT exhibits a Seebeck coefficient (~ 20–50 $\mu V K^{-1}$) larger than that of metallic polyaniline (~ + 10 $\mu V K^{-1}$)[3,23]. Accordingly, the low room-temperature Seebeck coefficient of PBFDO (-7 $\mu V K^{-1}$) together with its linear temperature dependence is consistent with metallic-like charge transport. While the negative sign indicates electron-dominated transport, it is not necessarily linked to the nominal doping polarity. Rather, the details of the doping-induced electronic structure at the Fermi level determine whether electrons or holes dominate thermoelectric transport. This is exemplified by p-doped conducting polymers that nevertheless display a negative Seebeck coefficient[26].

The magnetic susceptibility of spin-coated PBFDO films exhibits a temperature-independent response, characteristic of Pauli paramagnetism (Fig. 2c). This behaviour provides direct evidence for delocalized electronic states at the Fermi level[27] and is consistent with metallic electronic structures, in stark contrast to the Curie-like response expected for localized charge carriers in disordered conducting polymers[28].

A distinct plasmonic resonance at ~ 5.6 eV in the electron energy-loss spectrum (EELS)[29–32] of the PBFDO film provides further evidence of the delocalized free-carrier response underlying the metallic conductivity of PBFDO (Fig. 2d). The EELS plasmon originates from longitudinal bulk charge-density oscillations driven by momentum transfer from fast electrons, and differs from optically observed plasmons, which typically correspond to the lowest-energy plasmon modes (see SI, section 2, Fig. S2, Table S1).

Figure 3a presents the temperature-dependent electrical conductivity of spin-coated and drop-coated films (300 K-10 K), before and after ionic liquid (IL) treatment. The aprotic ionic liquid is 1-ethyl-3-methylimidazolium dicyanamide, whose bulky cation is unlikely to exchange with the protonic counterions that compensate the negative charges in n-doped PBFDO (Fig. S3). The untreated drop-coated film (black line) shows semiconducting behaviour with conductivity decreasing upon cooling.

IL treatment enhances its conductivity ~ 2.4-fold (blue line) and induces metallic behaviour, with a ~ 1.2-fold increase upon cooling, approaching 10,000 S cm^{-1} at low temperature. In contrast, the untreated spin-coated film already exhibits metallic transport with a ~ 2.2-fold rise in conductivity upon cooling (red line). After IL treatment, its conductivity increases by ~ 2.3-fold and the metallic character is strongly reinforced, reaching > 20,000 S cm^{-1} at 10 K (green line) (Table S2).

Figure 3b shows the EPR spectra of spin-coated and drop-coated PBFDO films. When normalized by film volume (Table S3), the EPR signal reveals that drop-coated films exhibit a spin density approximately one order of magnitude higher than that of spin-coated films. This observation suggests that higher polaron densities are associated with increased molecular disorder, consistent with the structural differences evidenced by XRD measurements (Fig. 4). Following the IL treatment, the EPR signals of both drop-coated and spin-coated films become nearly undetectable, indicating the effective disappearance of polarons. In the Discussion, we propose the reorganization of protons as the principal mechanism underlying this phenomenon.

Metals exhibit high visible-light reflectance owing to their large density of mobile charge carriers (~ 10^{23} cm^{-3}), which generate surface currents that screen incident electromagnetic fields. In conducting polymers, the lower carrier density (~ 10^{21} cm^{-3}), caused by larger repeat units and interchain spacing, shifts this metallic-type reflectance to the IR range. In drop-coated PBFDO films (~ 3 μm thick), strong reflectance is observed below 2 eV (black curve, Fig. 3c)[2,6,33]. After IL treatment, the reflectance increases, indicating a higher charge-carrier density (blue curve, Fig. 3c). As the photon energy increases, the electromagnetic wave couples more efficiently to the collective motion of the π-electron “gas” against the positively charged ionic background of the lattice. This coupling enhances absorption of the incident radiation and produces a minimum in the reflectance spectrum around 2 eV, commonly referred to as the plasma edge. Previous work has shown that nano-patterned PBFDO exhibits a plasmon frequency that shifts with the pattern dimensions[34], providing further evidence that π-electron plasmons exist in doped PBFDO.

In the absorption spectrum (Fig. 3d) of the spin-coated films (thickness = 300 Å), the plasma edge at 620 nm (corresponding to 2 eV in the reflectance spectrum) marks the onset of a broad infrared absorption background. The absorption features at 500 nm and 850 nm, previously observed in partially de-doped PBFDO[34], are likely associated with π-π* transitions involving polaronic localized states as indicated by significant EPR signals on both drop-coated (black curve) and spin-coated films (red curve) (Fig. 3b). After IL treatment, however, these optical transitions vanish (green curve, Fig. 3d), concomitant with the loss of the EPR signal (green and blue curves in Fig. 3b). At the same time, a more prominent IR background emerges. These observations indicate suppression of polaronic levels. The emerging Drude-like absorption background can be assigned to low-energy transitions between the filled negative-bipolaron band and the first empty conduction band, or to transitions involving a partially filled conduction band. The disappearance of the EPR signal indicates the removal of localized spin-1/2 polarons, whereas the temperature-independent magnetic susceptibility reflects itinerant electronic

states at the Fermi level. Thus, the spin response distinguishes localized polaronic defects from the delocalized metallic band formed by the bipolaron network.

To directly correlate structure with transport (Fig. 3a), X-ray diffraction (XRD) and Grazing-incidence wide-angle X-ray scattering (GIWAXS)[35,36] measurements were performed (Fig. 4, Table S4). All films exhibit a dominant diffraction peak at 2θ ≈ 8.2°-8.5° (Fig. 4a, b, Fig. S4), corresponding to lamellar (100) stacking with *d*-spacings of 10.74 Å-10.36 Å. Upon IL treatment, this peak systematically shifts to higher angles (~ 0.1°) and increases in intensity, indicating a modest contraction of the lamellar spacing (~ 0.1 Å) together with enhanced crystallinity. This provides evidence that the cations of the ionic liquid do not replace the protons, as such substitution would be expected to increase the lamellar spacing by inserting species between the lamellae[10,21,37]. GIWAXS confirms this trend (Fig. S5): the out-of-plane profiles show lamellar spacings ($Q_z \approx 0.60$ Å^{-1}) decreasing from 10.65 Å to 9.65 Å across the series (Fig. 4c, Fig. S6), while preserving a predominantly edge-on orientation, with (100) reflections out-of-plane and π-π (010) stacking in-plane (Fig. 4d), as found in other reports[38,39].

More critically, the π-π stacking distance decreases slightly from ~ 3.31 Å in drop-coated films to ~ 3.27 Å in the IL-treated spin-coated film (Fig. 4d, Fig. S7). Although small, such a reduction places the system at the lower bound of reported π-π spacings for PBFDO and is expected to significantly enhance intermolecular electronic coupling, which decays exponentially with interchain distance[40]. This provides a structural basis for the transport evolution in Fig. 3: the drop-coated film, characterized by weaker order and larger intermolecular separation, remains semiconducting, whereas the more ordered spin-coated film with similar π-π stacking distance (3.30 Å) already exhibits metallic behaviour. IL treatment further reinforces metallic transport in both cases—most prominently in the spin-coated film (8300 S cm^{-1} at 300 K)—consistent with enhanced interchain coupling and carrier delocalization arising from both improved crystalline order and reduced π-π separation (3.27 Å)[6].

Discussion

We propose that IL treatment enhances metallicity through coupled structural and protonic reorganization: it promotes proton configurations that favor spinless negative bipolarons while improving the intermolecular packing needed to delocalize the bipolaron-derived states. The ionic environment of the IL screens proton–backbone electrostatic interactions, increasing proton mobility and enabling diffusion through the swollen film. Protons interacting with the C = O groups can occupy several local minima that stabilize negative charges on the π-electron system. Because protonation of a single C = O group breaks monomer symmetry, we denote the protonated side as the “head” (h) and the opposite side as the “tail” (t). Both oligomer-level DFT calculations[41] and robust 3D models of paired PBFDO chains (see SI 4.1, Fig. S8) identify the head-to-head (h-h) configuration as the global minimum, more stable by ~ 0.2 eV per unit cell (≈ 4.6 kcal mol^{-1}) than any alternative. In the oligomer models, the (h-h) configuration corresponds to a singlet state and is therefore bipolaronic, whereas the less stable (t-t) and (h-t) arrangements adopt triplet states characteristic of polaronic species[41] (Fig. S9). Therefore,

IL-induced swelling promotes proton diffusion that allows PBFDO nanocrystals to relax toward this lowest-energy arrangement, yielding regularly spaced bipolarons along the chains which suppress EPR response (Fig. 3b, green). In contrast, when proton mobility is limited during film formation, protons become trapped in local energy minima. These metastable configurations produce localized polarons that disrupt the delocalized π-electron system associated with the bipolaron network, giving rise to the EPR signal observed in untreated spin-coated films (Fig. 3b, red). The negative charges on the π-electron system, localized as negative polarons, become disconnected from the main negative bipolaron band, which reduces the density of delocalized mobile carriers. The extent of this disruption also depends on the degree of molecular order. When disorder is pronounced (Fig. 4a), the bipolaron network is strongly fragmented and the films exhibit thermally activated conductivity, as observed for untreated drop-coated films (Fig. 3a, black), which also display the strongest EPR signal. IL treatment of the drop-coated films likely improves molecular ordering (Fig. 4a) while enabling proton rearrangement toward the lowest-energy configuration. Therefore, polarons disappear and metallic conductivity emerges (Fig. 3a, blue).

The simplified level diagram in Fig. 1h treats the bipolaron-derived band and the modified conduction band schematically. We therefore constructed a 3D packing model to test whether realistic interchain coupling and bipolaron ordering instead produce a partially filled dispersive band. Because the head-to-head (h-h) protonated configuration is energetically favored, we constructed a three-dimensional structural model of the PBFDO packing in which the unit cell comprises two adjacent polymer chains (Fig. 5a), in which every second connection is a doubly protonated (h-h) site bearing two protons, one on each adjacent BFDO unit. In this description, the effective repeat unit consists of an alternating sequence of (h-h) protonated connections (bipolaron sites) and non-protonated connections (neutral regions) (Fig. S10-S15). In particular, Figures S12-S14 trace the HOMO/LUMO-derived orbitals from molecular fragments to the one-dimensional bipolaron-network limit. This periodic alternation defines a regular array of negative bipolaronic states along the polymer backbone. Importantly, the bipolaronic sites on one chain are not vertically aligned with those on neighboring chains along the π-π stacking direction. Instead, they are laterally shifted, resulting in a three-dimensionally distributed pattern of charges within the crystal.

Figure 5b shows that the bipolaron network exhibits metallic character, with partially filled bands crossing the Fermi level at the R and V k-points. This electronic structure is obtained using the π–π stacking distance extracted from GIWAXS (3.27 Å) together with a short lamellar spacing (7.53 Å), consistent with previous theoretical predictions[42]. The band anisotropy reveals strong dispersion along Γ→X (intrachain) and along Γ→R and Γ→V (intra-lamellar π-stacking), whereas the absence of dispersion along Γ→Z indicates negligible electronic coupling between lamellae. Wavefunction analysis further shows that states near the Fermi level originate from interactions between HOMO-derived orbitals of the repeat units (Figs. S10, S11, S16).

Increasing the π-π stacking distance from 3.27 Å to 3.90 Å eliminates the metallic character and opens a small indirect gap (Fig. 5b, c and Fig. S17), despite strong dispersion along Γ→X, showing that intrachain transport alone cannot sustain metallicity (Fig. S16). Moreover, a short π-π distance by itself is

insufficient: enlarging the lamellar spacing suppresses the metallic electronic structure (Fig. 5b, d, Fig. S18), demonstrating that charge transport in PBFDO is intrinsically three-dimensional rather than confined within individual lamellae. At the same time, the experimental observation of metallic conductivity in samples with a larger average lamellar spacing (9.65 Å), despite the absence of a metallic electronic structure in the corresponding model (Fig. S19), highlights the crucial role of structural disorder. XRD peak broadening indicates a distribution of interlamellar distances and chain orientations, enabling local regions with short separations (~ 7.5 Å) (Fig. 5d) and small rotational offsets that generate percolating metallic pathways across lamellae.

This refined model reconciles the key experimental observations. The bipolaron network, consistent with the absence of an EPR signal (Fig. 3b), gives rise to a genuinely metallic electronic structure, accompanied by temperature dependences of the conductivity and Seebeck coefficient that are characteristic of metals (Fig. 2a, b and 3a). If the Fermi level were instead positioned, as illustrated in Fig. 1h, at the boundary between the filled and empty bands, the Seebeck coefficient would be expected to be significantly larger, and the resulting electronic structure would correspond to a semimetal rather than a metal. This work establishes that an n-doped polymer hosts metallic transport through a negative-bipolaron-derived band when proton configuration and intermolecular coupling are jointly optimized. The model explains the combined transport, spin, optical and structural observations, while also showing that disorder and lamellar spacing remain limiting factors.

Methods

General procedure for the synthesis of PBFDO

3,7-dihydrobenzo[1,2-b:4,5-b']difuran-2,6-dione (H-BFDO) crystals and duroquinone (TMQ) (1.6 eq) were dissolved in extra-dry DMSO (about 15 mg ml^{-1} for H-BFDO) under a nitrogen environment. The reaction mixture was heated at 100 °C for ~ 1 h and the mixture was cooled to room temperature, at which point a gel formed. Afterward, the solution was dialyzed using a dialysis bag with a cutoff molecular weight of 10 kDa (Viskase, USA) to remove the low molecular weight portion. The resulting solution was filtered by a 0.45 μm polytetrafluoroethylene filter (25 mm, SCAA-205, ANPEL Laboratory Technologies (Shanghai) Inc.) using a syringe and then concentrated to a final concentration of 10 ± 2 mg ml^{-1}. The solution was kept in the glove box for further characterization.

A detailed example of the reaction is below. H-BFDO crystals (160 mg, 0.84 mmol, 1 equiv) and TMQ crystals (221 mg, 1.35 mmol, 1.6 equiv) were fully deoxygenated in a glove box and then dissolved in 10 ml DMSO (Extra Dry, 99.7%). Afterwards, the reaction mixture was heated to 100 °C with vigorous stirring. The solution gradually changed from pale yellow to dark brown. After about 1 h, a marked increase in viscosity could be observed and the reaction mixture was cooled to room temperature. Another 2 ml of DMSO was injected to dilute the mixture and the reaction solution was

transferred into the dialysis bag, which was pretreated with deionized water. The dialysis bag was submerged in the pure DMSO (Extra Dry, 99.7%) solution for dialysis. The DMSO solution was changed once per day and the whole process took about 5 days until the DMSO solution outside the dialysis bag became colorless. Then the polymer solution in the dialysis bag was collected and filtered by a 0.45-μm polytetrafluoroethylene filter using a syringe. Finally, 200 μL of the resulting solution was taken and the final concentration was confirmed through weighing solids after complete removal of DMSO.

The synthesis of PBFDO using SeO_2 and $Cu(OAc)_2$ catalysts followed the same procedures as reported in the literature. The conducting solution PBFDO was provided by Dongguan Volt-Amp Optoelectronics Technology Co., Ltd.

Film deposition

Spin-coated film

The solution of PBFDO (10 ± 2 mg ml^{-1} in DMSO) was dropped on the pre-cleaned substrate in the glove box. The spin-coated films were prepared by the off-center spin-coating method at various rates. The desired thickness was achieved by controlling the rotation rates. The film was heated at 80 °C in the glove box for 1.5 h. The substrate was then carefully transferred to a vacuum box and heated at 60 °C under vacuum for 12 h to remove the solvent. The thickness of the film was measured using an Ambios Technology XP-2 profilometer.

Drop-coated film

The solution of PBFDO (10 ± 2 mg ml^{-1} in DMSO) was dropped on the pre-cleaned substrate in the glove box. The film was heated at 80 °C in the glove box for 2 h. The substrate was then carefully transferred to a vacuum box and heated at 60 °C under vacuum for 12 h to remove the solvent. The thickness of the film was measured using an Ambios Technology XP-2 profilometer.

Ionic liquid treatment

For ionic liquid-treated films, as-coated substrates were transferred to a hotplate preheated to 80 ℃ inside an N_2-filled glove box (O_2 < 0.1 ppm, H_2O < 0.1 ppm). A 100 μL aliquot of 1-ethyl-3-methylimidazolium dicyanamide (EMIM:DCA) solution was dispensed onto the substrate and held for 30 s. The substrates were then transferred to a spin coater, where residual ionic liquid was removed by high-speed spinning. During this step, the surface was concurrently rinsed with dimethyl sulfoxide (DMSO) to eliminate remaining residues. Post-treatment, the substrate was then carefully transferred to a vacuum box and heated at 60 °C under vacuum for 12 h to remove the solvent, followed by characterization.

Transport measurement

The temperature-dependent resistance was measured in a four-probe geometry using the PPMS (EverCool-II, Quantum Design) at South China University of Technology. The film was coated on a quartz

substrate with electrodes (base contact), and the electrodes consisted of pre-deposited 30-nm Cr and 100-nm Au. The electrical conductivity was measured by the van der Pauw method from the 1mm×1 mm square film.

SEM

The top surface image of the thin film was acquired using a high-resolution cold field emission scanning electron microscope (Hitachi Regulus 8100). The acceleration voltage was set to 5 kV, and the working distance was maintained at 9.2 mm. The sample was sputter-coated with platinum before measurements.

Thermoelectric performance

Seebeck coefficient measurements were performed using the thermal transport option (TTO) of a Quantum Design PPMS (DynaCool 9T) at Jiangxi Science and Technology Normal University.

Magnetic susceptibility

Magnetic susceptibility was measured using a vibrating sample magnetometer (VSM) attached to the PPMS (EverCool-II, Quantum Design) at South China University of Technology.

Electron energy loss spectrum

Electron energy loss spectrum measurements were performed at GATAN Continuum ER/1065 energy filtering system of Talos F200X G2 at South China University of Technology. The energy dispersion parameter was selected as 15 meV. The convergence semi-angle is 9.6 mrad, and the collection semi-angle is 42 mrad. Raw spectra were first corrected using the built-in tools of the GATAN Digital Micrograph software to account for any drift in energy experienced during the scan by aligning the zero-loss peak maximum at 0 eV. The plasmon peaks of the material were fitted using the Gaussian function.

Electron paramagnetic resonance

Electron paramagnetic resonance measurements of the spin-coated and drop-coated films were performed on a Bruker E500 spectrometer at a microwave frequency of approximately 9.8 GHz. To eliminate the signal differences arising from sample volume, we measured the film thickness and calculated the effective volume of the films. We normalized the EPR test signals based on the film volume to enable a reliable comparison between the drop-coated films and the spin-coated films.

Reflectance spectroscopy

Reflectance spectra of the drop-coated film were acquired on a SHIMADZU UV-3600 spectrophotometer in the 300–2500 nm range using an integrating sphere accessory. The film was drop-coated on a quartz substrate, and $BaSO_4$ was used as the background standard.

UV–vis–NIR absorption spectroscopy

The UV–vis–NIR absorption spectrum of the spin-coated film was collected on a SHIMADZU UV-3600 spectrophotometer over the wavelength range of 300–2500 nm. The film was deposited on a quartz substrate by spin-coating prior to measurement.

X-ray diffraction

X-ray diffraction measurements were performed on a Rigaku MiniFlex600 diffractometer. Data were collected in the 2Theta range of 3-40° with a step size of 0.01° and a scan rate of 5° min^{-1}. The films were deposited on silicon substrates for the measurements.

GIWAXS

2D GIWAXS measurements were carried out on the French Xenocs 2.0 instrument at South China University of Technology. The X-ray source was MetalJet-D2, Excillum with an incident angle of 0.2°. The X-ray wavelength was 0.134144 nm, and the scattering was detected using the Pilatus3R 1M photodetector.

Theoretical Calculations

Periodic density functional theory calculations were carried out with the QUICKSTEP module of the CP2K[43–45] package (version 2024.1). Structural optimization was performed under three-dimensional (3D) periodic boundary conditions by simultaneous optimization of the atomic positions and lattice parameters. The PBE exchange-correlation functional[46], together with the DFT-D3(BJ) dispersion correction[47], was employed for the structure optimization. Core-valence interactions were modeled with Goedecker–Teter–Hutter (GTH) pseudopotentials, and the valence states were expanded in TZV2P-MOLOPT-GTH basis sets[48,49]. The electron density was represented on a multigrid with a plane-wave cutoff of 400 Ry and a relative cutoff of 55 Ry. For the structural optimizations of the 3D PBFDO bipolaron network structures, Monkhorst-Pack k-point meshes of 5×15×5 were adopted, while the corresponding meshes for the subsequent self-consistent electronic-structure calculations were 9×25×9. The self-consistent field procedure was converged using an SCF convergence threshold of 1.0×10-6 a.u., and Fermi-Dirac smearing at an electronic temperature of 300 K. Cell optimization was carried out under an external pressure of 1.01325 bar, while preserving the crystal symmetry and space group. The density of states and band structures were obtained from single-point electronic-structure calculations on the optimized structure using the HLE17 functional[50], with the same basis sets and pseudopotentials as those used in the geometry optimization. For band-structure calculations, the high-symmetry k-point paths were generated using SeeK-path tools[51,52].

To further examine the real-space distribution of the molecular orbitals associated with the optimized PBFDO structure, a finite molecular fragment was extracted from the optimized 3D periodic structure. The dangling bonds generated by truncating the periodic framework were saturated with H atoms.

Single-point molecular orbital calculations were then performed for the hydrogen-terminated finite model using the intermediate neglect of differential overlap (INDO) semiempirical Hamiltonian[53] implemented in Gaussian 16[54]. The resulting checkpoint file was converted to a formatted checkpoint file and analyzed with Multiwfn[55,56]. Selected molecular orbitals were exported as volumetric cube files and visualized as isosurfaces using VESTA[57]. These finite-cluster INDO calculations were used to provide an intuitive molecular-orbital representation of the local electronic structure.

Declarations

Acknowledgements

This work was financially supported by the Natural Science Foundation of China (92463310, 22575091 and 52203221), the Wallenberg Initiative Materials Science for Sustainability (WISE) and the Swedish Government Strategic Research Area in Materials Science on Advanced Functional Materials at Linköping University (Faculty Grant SFO-Mat-LiU no. 2009-00971). The authors thank Dr. Ximei Liu from Jiangxi Science and Technology Normal University for the thermoelectric measurement. The authors thank Dr. Jie Cui and Dr. Xianfeng Yang from the Analytical and Testing Centre of South China University of Technology for performing the EELS characterization. The authors thank Dr. Xiaojuan Ni and Prof. Jean-Luc Brédas for generously providing the band-structure data from their PBFDO study, which provided valuable reference for this work.

Author contributions

Y.M., Q.J., R.C. and J.Z. proposed and supervised the whole research. S.T., Q.J. and J. Z. designed the experiments. S.T. carried out the preparation and characterization of the films. J.Z. and S.T. performed transport and magnetic measurements. H.G. conducted DFT calculations. M.S., H.P., Z.Q., W.C., Y.Z., J.Y. and N.Z. provided assistance in the film characterization. S.T. and R.C. drafted the initial manuscript. S.T., H.G., Q.J. and J.Z. revised the manuscript with the input of R.C., H.U., L.Y., H.T., F.H. and Y.M. All authors engaged in discussions on the results and provided comments on the paper.

Competing Interests

The authors declare that they have no competing financial interests.

Data availability

The data that support the findings of this study are available from the corresponding author on reasonable request.

References

1. Kang, S. D. & Snyder, G. J. Charge-transport model for conducting polymers. *Nat. Mater.* **16**, 252–257 (2017).
2. Lee, K. *et al.* Metallic transport in polyaniline. *Nature* **441**, 65–68 (2006).
3. Bubnova, O. *et al.* Semi-metallic polymers. *Nat. Mater.* **13**, 190–194 (2014).
4. Guo, Z. *et al.* Semimetallization induced Hall anomaly in doped polymers. *Phys. Rev. Res.* **6**, 043180 (2024).
5. Zhang, T. *et al.* Two-dimensional polyaniline crystal with metallic out-of-plane conductivity. *Nature* **638**, 411–417 (2025).
6. Kim, N. *et al.* Role of Interchain Coupling in the Metallic State of Conducting Polymers. *Phys. Rev. Lett.* **109**, 106405 (2012).
7. Tang, H. *et al.* A solution-processed n-type conducting polymer with ultrahigh conductivity. *Nature* **611**, 271–277 (2022).
8. Ke, Z. *et al.* Highly Conductive and Solution-Processable n-Doped Transparent Organic Conductor. *J. Am. Chem. Soc.* **145**, 3706–3715 (2023).
9. Liu, G. *et al.* Selenium Dioxide Catalyzed Polymerization of N-doped Poly(benzodifurandione) (n-PBDF) and Its Derivatives. *Angew. Chem. Int. Ed.* **64**, e202418668 (2025).
10. Li, Z. *et al.* Practical lithium–organic batteries enabled by an n-type conducting polymer. *Nature* **651**, 100–106 (2026).
11. Koller, G. *et al.* Intra- and Intermolecular Band Dispersion in an Organic Crystal. *Science* **317**, 351–355 (2007).
12. Nowak, M., Rughooputh, S. D. D. V., Hotta, S. & Heeger, A. J. Polarons and bipolarons on a conducting polymer in solution. *Macromolecules* **20**, 965–968 (1987).
13. Brédas, J. L., Wudl, F. & Heeger, A. J. Polarons and bipolarons in doped polythiophene: A theoretical investigation. *Solid State Commun.* **63**, 577–580 (1987).
14. Cornil, J. & Brédas, J.-L. Nature of the optical transitions in charged oligothiophenes. *Adv. Mater.* **7**, 295–297 (1995).
15. Brédas, J. L. & Street, G. B. Polarons, bipolarons, and solitons in conducting polymers. *Acc. Chem. Res.* **18**, 309–315 (1985).
16. Crispin, X. *et al.* The Origin of the High Conductivity of Poly(3,4-ethylenedioxythiophene) –Poly(styrenesulfonate) (PEDOT–PSS) Plastic Electrodes. *Chem. Mater.* **18**, 4354–4360 (2006).
17. Chen, M. *et al.* Long-range extended chains arising from polymerization-driven spontaneous assembly. *Science* eaef1777 (2026).
18. Arkhipov, V. I., Emelianova, E. V., Heremans, P. & Bässler, H. Analytic model of carrier mobility in doped disordered organic semiconductors. *Phys. Rev. B* **72**, 235202 (2005).
19. Brédas, J. L., Themans, B., Andre, J. M., Chance, R. R. & Silbey, R. The role of mobile organic radicals and ions (solitons, polarons and bipolarons) in the transport properties of doped conjugated polymers. *Synth. Met.* **9**, 265–274 (1984).

20. Fahlman, M. *et al.* Experimental and theoretical studies of the electronic structure of Na-doped poly (para-phenylenevinylene). *Chem. Phys. Lett.* **214**, 327–332 (1993).
21. Lee, J. G. *et al.* High-Performance n-Type Thermoelectric Polymers via Ion-Exchange Tuning of Polaron–Cation Interactions. *Small* **22**, e11108 (2026).
22. Cutler, M. & Mott, N. F. Observation of Anderson Localization in an Electron Gas. *Phys. Rev.* **181**, 1336–1340 (1969).
23. Yoon, C. O., Reghu, M., Moses, D., Heeger, A. J. & Cao, Y. Counterion-induced processibility of polyaniline: Thermoelectric power. *Phys. Rev. B* **48**, 14080–14084 (1993).
24. Park, Y. W. Structure and morphology: relation to thermopower properties of conductive polymers. *Synth. Met.* **45**, 173–182 (1991).
25. Markov, M., Rezaei, S. E., Sadeghi, S. N., Esfarjani, K. & Zebarjadi, M. Thermoelectric properties of semimetals. *Phys. Rev. Mater.* **3**, 095401 (2019).
26. Liang, Z. *et al.* n-type charge transport in heavily p-doped polymers. *Nat. Mater.* **20**, 518–524 (2021).
27. Moraes, F. *et al.* Doped poly(thiophene): Electron spin resonance determination of the magnetic susceptibility. *Synth. Met.* **10**, 169–179 (1985).
28. Kang, K. *et al.* 2D coherent charge transport in highly ordered conducting polymers doped by solid state diffusion. *Nat. Mater.* **15**, 896–902 (2016).
29. Fink, J., Nücker, N., Scheerer, B. & Neugebauer, H. Investigation of thiophene-based conducting polymers by electron diffraction and by electron energy-loss spectroscopy. *Synth. Met.* **18**, 163–168 (1987).
30. Noriega, R. *et al.* A general relationship between disorder, aggregation and charge transport in conjugated polymers. *Nat. Mater.* **12**, 1038–1044 (2013).
31. Bhattacharya, S. *et al.* Intervalence plasmons in boron-doped diamond. *Nat. Commun.* **16**, 444 (2025).
32. Zeng, F. *et al.* Two-Dimensional Electron Transport in N-Type Conducting Polymers by Dication Exchange. *J. Am. Chem. Soc.* **148**, 9358–9366 (2026).
33. Lee, K. & Heeger, A. J. Optical investigation of intra and interchain charge dynamics in conducting polymers. *Synth. Met.* **128**, 279–282 (2002).
34. Kazi, S. *et al.* n-Type redox-tuneable conducting polymer optical nanoantennas. *J. Mater. Chem. C* **12**, 17469–17474 (2024).
35. Joseph Kline, R., McGehee, M. D. & Toney, M. F. Highly oriented crystals at the buried interface in polythiophene thin-film transistors. *Nat. Mater.* **5**, 222–228 (2006).
36. Rivnay, J., Mannsfeld, S. C. B., Miller, C. E., Salleo, A. & Toney, M. F. Quantitative Determination of Organic Semiconductor Microstructure from the Molecular to Device Scale. *Chem. Rev.* **112**, 5488–5519 (2012).
37. Zhang, J. *et al.* Trace Dual-Crosslinkable Additives Enable Direct Microlithography for Enhanced Organic Electrochemical Transistors. *Adv. Mater.* **37**, 2417452 (2025).

38. Zhao, Y. *et al.* Environmentally Stable N-Type Conducting Polymer with High Intrinsic Stretchability. *Adv. Mater.* **38**, e18190 (2026).
39. Li, Q. *et al.* A water-processable n-type polymeric ink with conductivities exceeding 1,000 S cm−1. *Matter* **9**, 102599 (2026).
40. Bhat, V., Ganapathysubramanian, B. & Risko, C. Rapid Estimation of the Intermolecular Electronic Couplings and Charge-Carrier Mobilities of Crystalline Molecular Organic Semiconductors through a Machine Learning Pipeline. *J. Phys. Chem. Lett.* **15**, 7206–7213 (2024).
41. Ni, X., Li, H. & Brédas, J.-L. Electronic and Magnetic Properties of Oligomers and Chains of Poly(benzodifurandione) (PBDF), A Highly Conducting n-Type Polymer. *Chem. Mater.* **35**, 5886–5894 (2023).
42. Ni, X., Li, H., Coropceanu, V. & Brédas, J.-L. Dimensionality-Dependent Electronic Properties of the Highly Conducting n-Type Polymer, Poly(benzodifurandione). *ACS Mater. Lett.* **6**, 2569–2576 (2024).
43. Kühne, T. D. *et al.* CP2K: An electronic structure and molecular dynamics software package - Quickstep: Efficient and accurate electronic structure calculations. *J. Chem. Phys.* **152**, 194103 (2020).
44. Hutter, J., Iannuzzi, M., Schiffmann, F. & VandeVondele, J. cp2k: atomistic simulations of condensed matter systems. *WIREs Comput. Mol. Sci.* **4**, 15–25 (2014).
45. VandeVondele, J. *et al.* Quickstep: Fast and accurate density functional calculations using a mixed Gaussian and plane waves approach. *Comput. Phys. Commun.* **167**, 103–128 (2005).
46. Perdew, J. P., Burke, K. & Ernzerhof, M. Generalized Gradient Approximation Made Simple. *Phys. Rev. Lett.* **77**, 3865–3868 (1996).
47. Grimme, S., Ehrlich, S. & Goerigk, L. Effect of the damping function in dispersion corrected density functional theory. *J. Comput. Chem.* **32**, 1456–1465 (2011).
48. Goedecker, S., Teter, M. & Hutter, J. Separable dual-space Gaussian pseudopotentials. *Phys. Rev. B* **54**, 1703–1710 (1996).
49. VandeVondele, J. & Hutter, J. Gaussian basis sets for accurate calculations on molecular systems in gas and condensed phases. *J. Chem. Phys.* **127**, 114105 (2007).
50. Verma, P. & Truhlar, D. G. HLE17: An Improved Local Exchange–Correlation Functional for Computing Semiconductor Band Gaps and Molecular Excitation Energies. *J. Phys. Chem. C* **121**, 7144–7154 (2017).
51. Hinuma, Y., Pizzi, G., Kumagai, Y., Oba, F. & Tanaka, I. Band structure diagram paths based on crystallography. *Comput. Mater. Sci.* **128**, 140–184 (2017).
52. Togo, A., Shinohara, K. & Tanaka, I. Spglib: a software library for crystal symmetry search. *Sci. Technol. Adv. Mater. Methods* **4**, 2384822 (2024).
53. Pople, J. A., Beveridge, D. L. & Dobosh, P. A. Approximate Self-Consistent Molecular-Orbital Theory. V. Intermediate Neglect of Differential Overlap. *J. Chem. Phys.* **47**, 2026–2033 (1967).
54. Frisch, M. J. *et al.* Gaussian˜16 Revision C.01. (2016).

55. Lu, T. & Chen, F. Multiwfn: A multifunctional wavefunction analyzer. *J. Comput. Chem.* **33**, 580–592 (2012).
56. Lu, T. A comprehensive electron wavefunction analysis toolbox for chemists, Multiwfn. *J. Chem. Phys.* **161**, 082503 (2024).
57. Momma, K. & Izumi, F. *VESTA 3* for three-dimensional visualization of crystal, volumetric and morphology data. *J. Appl. Crystallogr.* **44**, 1272–1276 (2011).

Figures

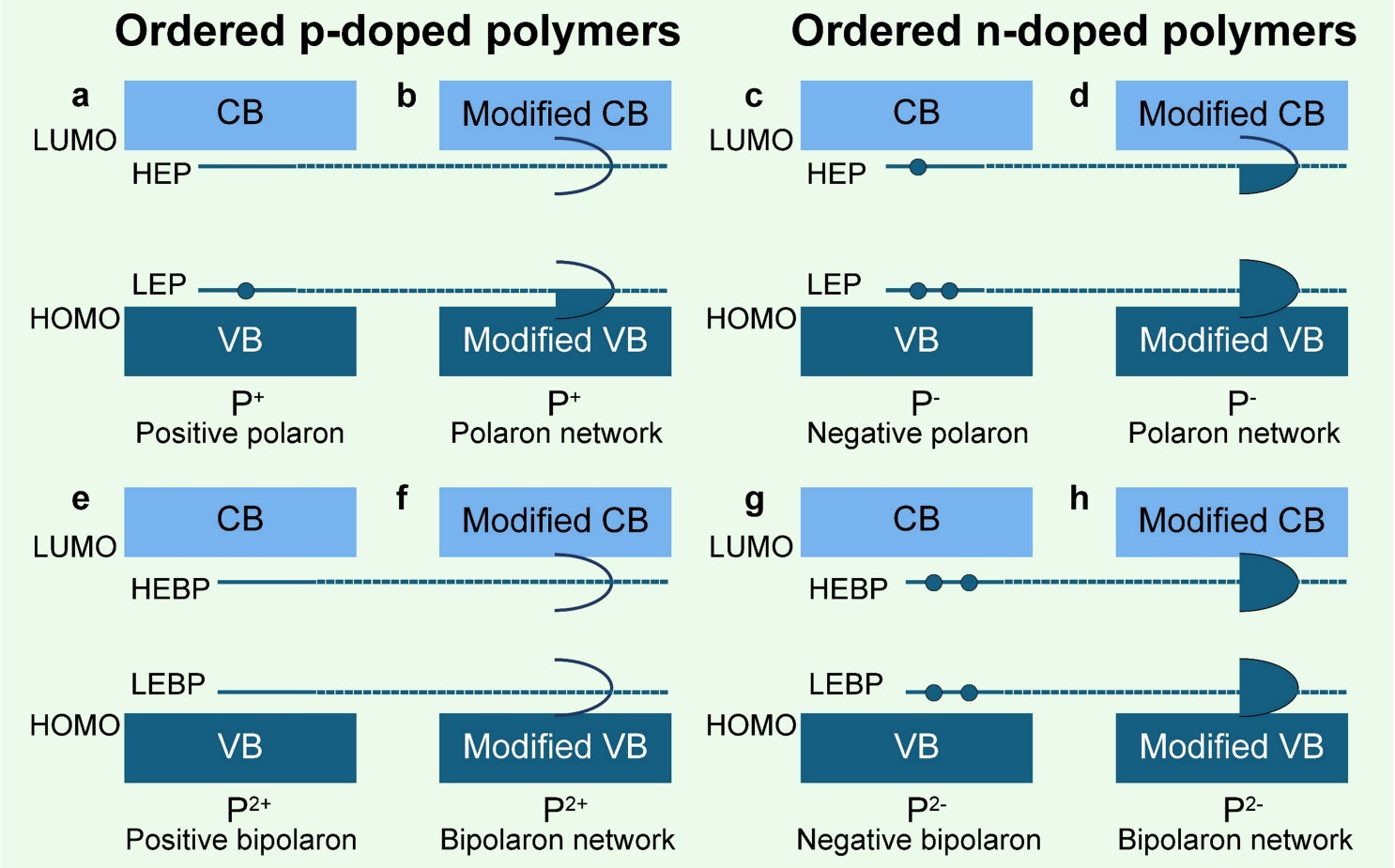


Figure 1

Electronic structure of n- and p-dopedcharge species and the resulting delocalized bands at high doping levelsin the presence of significant interchain coupling. a, Positive polaron (radical cation). **b**, Positive polaron network is a metal with a half-filled, delocalized positive polaron band. **c**, Negative polaron (radical anion). **d**, Negative polaron network is a metal with a half-filled, delocalized negative polaron band at high energy. **e**, Positive bipolaron (dication). **f**, Positive bipolaron network is a semimetal with the empty low-energy bipolaron band overlapping with the top of a modified valence band (modified means it is not the VB of the undoped system). **g**, Negative bipolaron (dianion). **h**, Negative bipolaron

network is a semimetal with the formation of a delocalized negative bipolaron band overlapping with a modified empty conduction band.

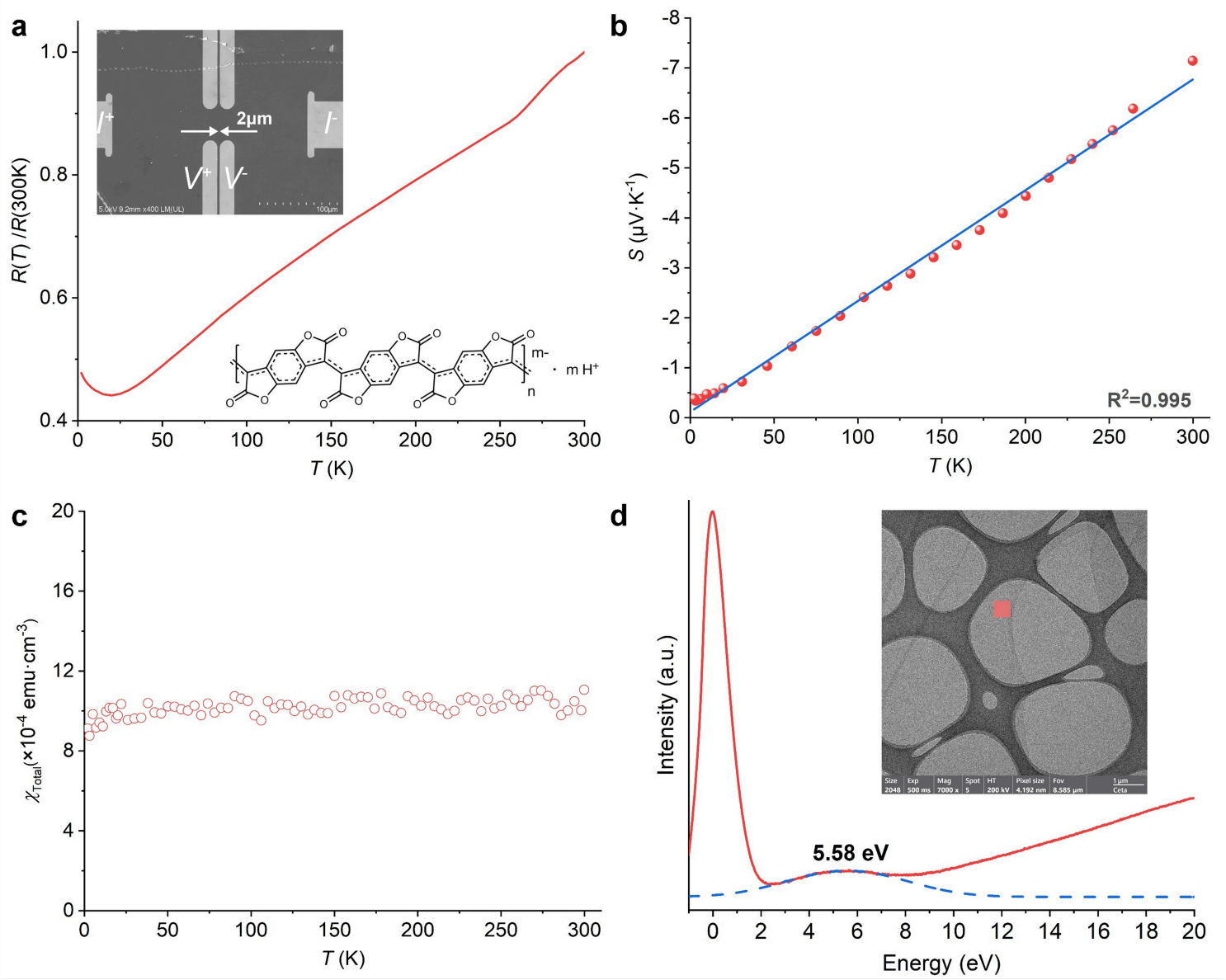


Figure 2

Evidence of metallic state of spin-coated PBFDO films. a, Temperature dependence of resistance (normalized to 300 K), the chemical structure of PBFDO and the SEM image of the electrode pattern with 2 μm channel (as shown in the inset). **b**, Temperature dependence of Seebeck coefficient and linear data fitting, the test schematic diagram (as shown in the inset). **c**, Temperature dependence of magnetic susceptibility. **d**, Electron energy loss spectrum of PBFDO film and its plasmon peak fitting. (The inset shows the TEM image).

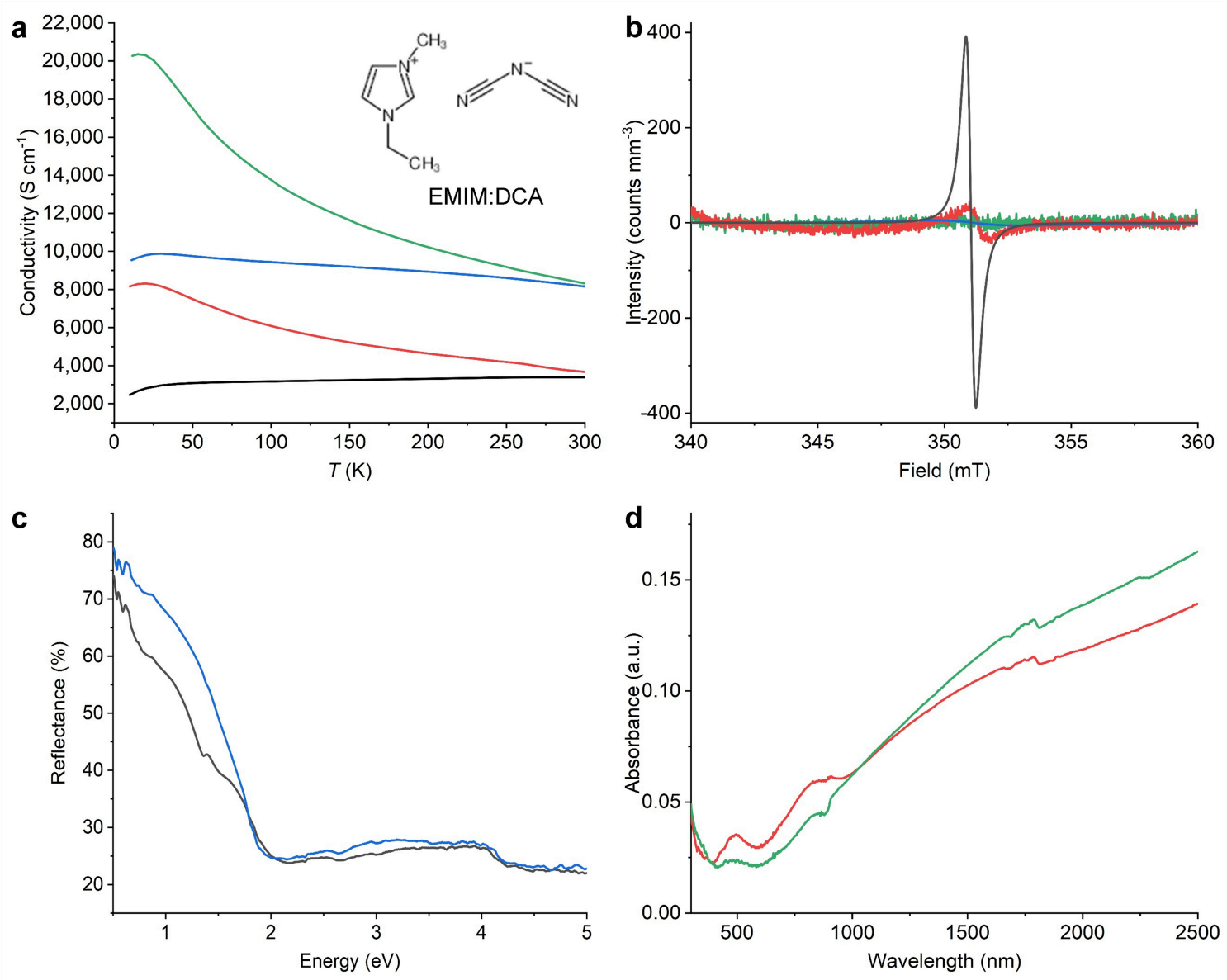


Figure 3

Effects of IL on the structure and properties of PBFDO films. a, Temperature dependence of the electrical conductivity for (i) drop-coated PBFDO (black), (ii) IL-treated drop-coated PBFDO (blue), (iii) spin-coated PBFDO (red), (iv) IL-treated spin-coated PBFDO (green). The chemical structure of ionic liquid is shown in the inset. **b**, EPR for (i) drop-coated PBFDO (black), (ii) IL-treated drop-coated PBFDO (blue), (iii) spin-coated PBFDO (red), (iv) IL-treated spin-coated PBFDO (green). **c**, Reflectance spectra for drop-coated PBFDO (black), IL-treated drop-coated PBFDO (blue). **d**, Absorbance spectra for spin-coated PBFDO (red), IL-treated spin-coated PBFDO (green).

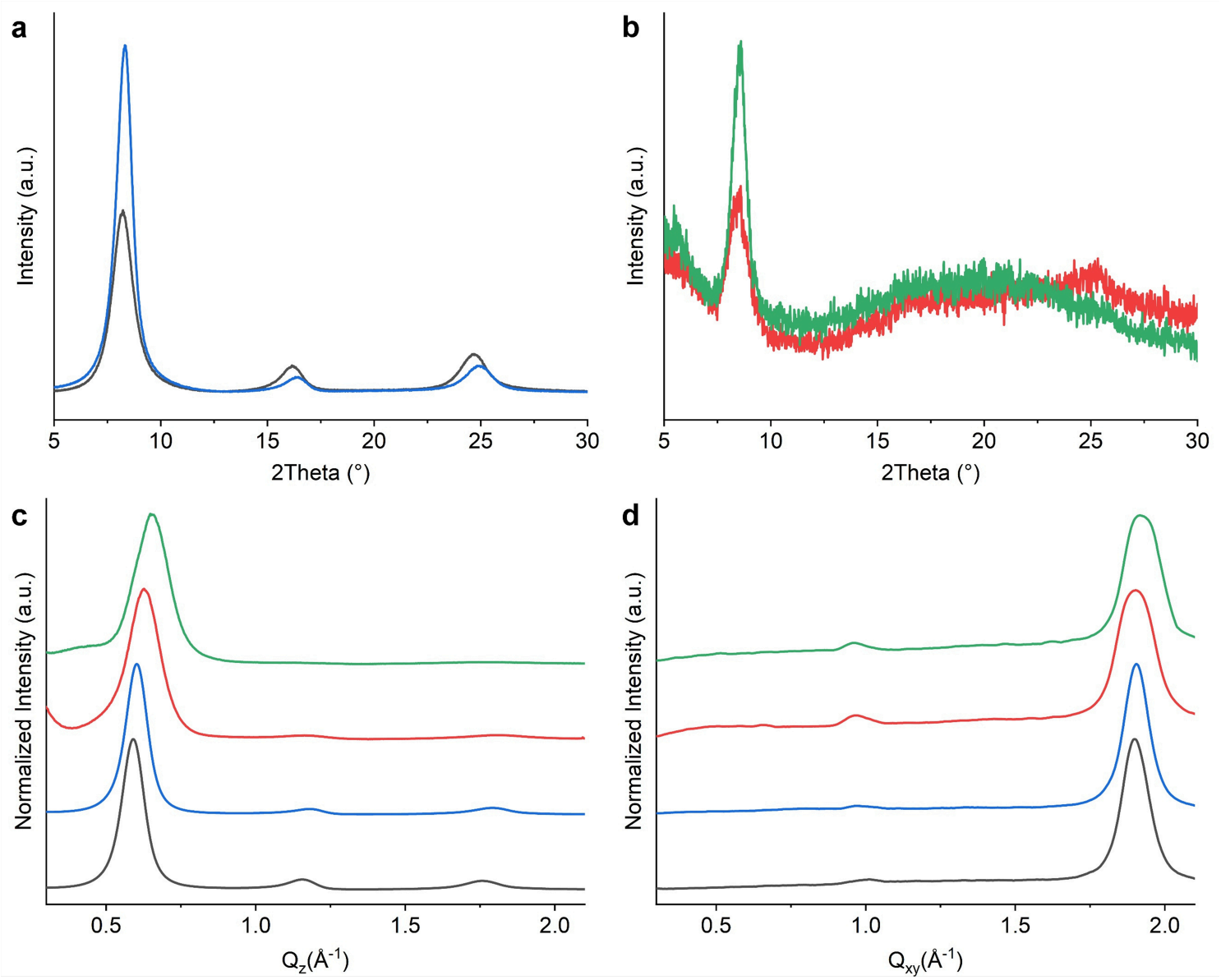


Figure 4

Structural analysis of PBFDO films by XRD and GIWAXS. a, Comparison of XRD of PBFDO drop-coated films before (black) and after (blue) IL treatment. **b**, Comparison of XRD of PBFDO spin-coated films before (red) and after (green) IL treatment. **c**, Q_z lamellar packing (100) and **d**, Q_{xy} π-π packing (010), for (i) Drop-coated PBFDO (black), (ii) IL-treated drop-coated PBFDO (blue), (iii) Spin-coated PBFDO (red), (iv) IL-treated spin-coated PBFDO (green).

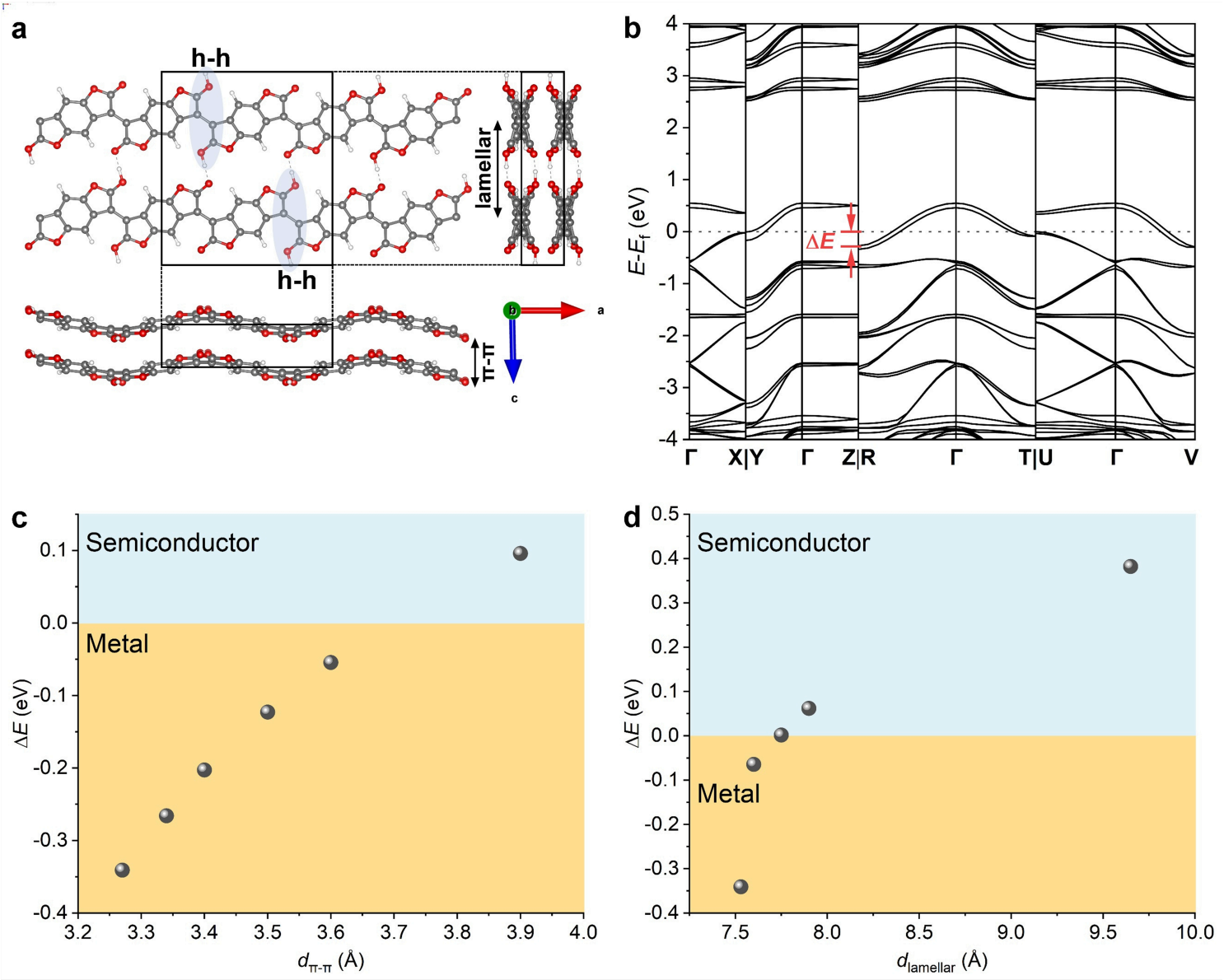


Figure 5

Electronic structure of the bipolaron network. a, Unit cell used in the 3D model of the bipolaron network ($d_{lamellar}$ = 7.53 Å, $d_{\pi\text{-}\pi}$ = 3.27 Å). **b**, Electronic band structure from periodic DFT calculations; ΔE denotes the energy difference at the R point between the valence band and the Fermi level. **c**, Evolution of ΔE as $d_{\pi\text{-}\pi}$ increases, showing the transition from metallic to semiconducting behaviour as a gap opens at ΔE = 0. **d**, Evolution of ΔE as $d_{lamellar}$ increases, likewise revealing the metallic-to-semiconductor crossover.

Supplementary Files

This is a list of supplementary files associated with this preprint. Click to download.

- Supplementaryinformation.docx